Research Article Vol. 31, No. 7 / 27 Mar 2023 / Optics Express 11053

Optics EXPRESS

Nonparaxial propagation and the radiation forces of the chirped circular Airy derivative beams

JIAN YU,[1] YIPING WANG,[2,*] ZHIYONG BAI,[2] LUPING WU,[2] CAILING FU,[2] SHEN LIU,[2] AND YU LIU[1]

[1] *Chongqing Engineering Research Center of Intelligent Sensing Technology and Microsystem, Chongqing University of Post and Telecommunications, Chongqing 400065, China*
[2] *Key Laboratory of Optoelectronic Devices and Systems of Ministry of Education and Guangdong Province, College of Physics and Optoelectronic Engineering, Shenzhen University, Shenzhen 518060, China*
[*] *ypwang@szu.edu.cn*

Abstract: In this paper, we investigate the nonparaxial propagation dynamics of the chirped circular Airy derivative beams (CCADBs) based on vector angular spectrum method. In the case of nonparaxial propagation, the CCADBs still maintains excellent autofocusing performances. Derivative order and chirp factor are two important physical quantities of the CCADBs to regulate the nonparaxial propagation characteristics, such as focal length, focal depth and K-value. In the nonparaxial propagation model, the radiation force on a Rayleigh microsphere induced the CCADBs are also analyzed and discussed in detail. The results demonstrate that not all derivative order CCADBs can achieve stable microsphere trapping effect. The derivative order and chirp factor of the beam can be used to coarse and fine tune the capture effect of Rayleigh microsphere, respectively. This work will contribute to the more precise and flexible use of circular Airy derivative beams in optical manipulation, biomedical treatment and so on.

1. Introduction

Abruptly autofocusing (AFF) beams have attracted widespread attention in recent years due to their important applications in many fields such as particle manipulation, laser surgery, and high harmonics generation. A typical AFF beam is often referred to circular Airy beam (CAB), which was first described by the radially symmetric Airy function in 2010 [1]. It has been demonstrated that the CAB relied on radial Airy waves whose light intensity maintains quite low level during propagation until the focal point, where it abruptly increases by several orders of magnitude, and then it decreases with oscillation [2]. Subsequently, other different types of AFF beams following pre-engineered caustic trajectories have also been intensively studied through theory and experiments, especially the circle Pearcey beams and circle Swallowtail beams [3–6]. According to the caustic field theory, in essence, Airy beam, Pearcey beam, and Swallowtail beam belongs to the typical representative of the caustic field in different dimensions, respectively. Additionally, optical researchers also designed novel AFF beams by means of the non-catastrophe integral, such as the way to structure the polarization state and the way to add force symmetric perturbation [7,8].

Very recently, a novel kind of AFF beam namely circular Airy derivative beams (CADBs) was introduced through a combination of theoretical and experimental studies [9–11]. As an extension of CABs, the CADBs have a radial profile that is described by derivatives of the Airy function and exhibit stronger AFF ability than the CABs under the same conditions. Therefore, the CADBs could be more beneficial for particle trapping and manipulation in the field of optical tweezers to realize strong trapping stiffness. Nowadays, optical tweezers have become an indispensable tool to study the biological cells and viruses, DNA molecules, neutral atoms, and other particles

#484878 https://doi.org/10.1364/OE.484878
Journal © 2023 Received 3 Jan 2023; revised 2 Mar 2023; accepted 2 Mar 2023; published 17 Mar 2023

[12–15]. However, to our best knowledge, radiation forces induced the CADBs have not been studied before.

In most situations, the light beams used in optical tweezers must be small enough to trap particles. The waist radius of the CADBs at the focal point is typically on the order of wavelengths, so the paraxial propagation theory is no longer sufficiently accurate to calculate the radiation force on particles induced the CADBs, and the nonparaxial propagation theory has to be considered [16–19]. In this paper, we initially study the nonparaxial propagation dynamics of CADBs based on vector angular spectrum propagation theory. Then, we compare and analyze the calculation results under paraxial propagation and nonparaxial propagation, especially in terms of focal length, focal depth and K-value characteristics. Especially, we also investigate the influence of chirp parameters on the propagation characteristics of CADBs. Finally, we study the radiation force of the CCADBs exerted on a Rayleigh dielectric microsphere, and compare the trapping stability of the CCADBs to the microsphere under different derivative orders and chirp parameters.

2. Nonparaxial propagation theory of CCADBs

The electric field of CCADBs on the initial plane is described as

$$E(r,\varphi,z=0)=A_n exp\left[a\left(\frac{r_0-r}{w_0}\right)\right]Ai^{(n)}\left(\frac{r_0-r}{bw_0}\right)\exp\left(ic\frac{r}{w_0}\right), \quad (1)$$

where r is the radial coordinate, φ denotes an azimuthal angle, and z is the propagation distance. A_n is constant amplitude related to the optical power of CCADBs on the initial plane. r_0 is the radius of the primary ring, w_0 is a scaling factor, a is an exponential decay factor, b denotes a distribution factor parameter, and c represents the chirp coefficient. $Ai^{(n)}$ is the n^{th}-order derivative of Airy function with respect to r. If $n=0$ and $c=0$, the CCADBs reduces to the familiar CAB.

For simplicity, we consider the CCADBs on the initial plane is linearly polarized in the x direction. The nonparaxial propagation of the CCADBs in free space can be analyzed by using the vectorial angular spectrum method, and the expression of the electric field in the whole half-space $z>0$ can be given as:

$$U(r,\varphi,z)=E_x(r,z)\hat{x}+E_z(r,\varphi,z)\hat{z}, \quad (2)$$

where only light intensity is concerned, thus E_x (r, z) is not related to the azimuthal angle φ. In terms of angular spectrum propagation method, E_x (r, z) can be expressed as the following 0^{th}-order inverse Hankel transform form owing to the circular symmetry of CCADBs:

$$E_x(r,z)=H^{-1}{}_0[\hat{E}_x(f_r;z)], \quad (3)$$

$$\hat{E}_x(f_r;z)=\hat{E}_x(f_r;0)\exp\{i(2\pi/\lambda)z[1-(\lambda f_r)^2]^{1/2}\}, \quad (4)$$

$$\hat{E}_x(f_r,0)=H_0[E(r,0)], \quad (5)$$

where f_r is the spatial frequency, H_0 and $H^{-1}{}_0$ stand for the 0^{th}-order Hankel transform and inverse Hankel transform. We consider that there is no difference between the Hankel transform and the inverse Hankel transform in the mathematical form. $\hat{E}_x$ $(f_r; 0)$ is the angular spectrum of CCADBs on the initial plane $z=0$. Correspondingly, the E_z component can be expressed as:

$$E_z(r,z)=-iH_1{}^{-1}\left\{H_0[E(r,0)]\frac{f_r}{f_z}\exp\{i(2\pi/\lambda)z[1-(\lambda f_r)^2]^{1/2}\}\right\}\cos\varphi. \quad (6)$$

As we can see that the E_z component relates to the azimuth angle. On the initial plane, there is no asymmetry in the distribution of light intensity. However, with the increase of the propagation distance z, the intensity distribution of light field will no longer maintain the symmetry due to the influence of cosφ in E_z component. The asymmetry of intensity distribution will affect the symmetry of radiant force distribution on a Rayleigh dielectric microsphere. For simplicity, only the case of azimuth $\varphi = 0$ is examined in the following study.

In some cases it may be desirable and appropriate to take the paraxial (small-angle) approximation in Eq. (4):

$$(2\pi/\lambda)z[1-(\lambda f_r)^2]^{1/2} = (2\pi/\lambda)z[1-(\lambda f_r)^2/2]. \tag{7}$$

In addition, the E_z component in Eq. (2) is negligible in the case of paraxial approximation. Thus, the electric field $E\ (r, z)$ in the paraxial approximation can be expressed as:

$$E(r,z) = (1/4\pi^2)H^{-1}{}_0\{H_0[E(r,0)]\exp[i(2\pi/\lambda)z]\exp(-i\pi\lambda {f_r}^2 z)\}, \tag{8}$$

The intensity of the CCADBs can be described as follows:

$$I = |E_x(r,z)|^2 + |E_z(r,\varphi,z)|^2. \tag{9}$$

It is difficult to obtain the analytic expression for the intensity I. Here we use the quasi-discrete method proposed by Guizar-Sicairos *et al*. [20] to numerically calculate the Hankel transforms in Eqs. (3)-(9). The method originally proposed by Yu *et al*. [21] for evaluating the zero-order Hankel transform is generalized to high-order Hankel transforms. Compared to the existing methods, the quasi-discrete Hankel transforms method has been demonstrated to have higher accuracy and computational efficiency.

3. Propagation characteristics

In this section, we study the dynamic characteristics of nonparaxial propagation of CCADBs through numerical examples, such as focal length, focal depth, and K-value. Especially, we investigate the influence of different chirp parameters on propagation dynamics. In subsequent studies and calculations, we first assume $a = 0.2$, $b = 0.15$, $c = 0$, $w_0 = 10\,\mu$m, $r_0 = 50\,\mu$m, $\lambda = 632.8$ nm, and the incident power is set to 1 W. Unless otherwise specified, these assumed parameters will remain constant.

3.1. Distribution characteristics of light intensity on the initial plane

Figure 1 shows the light intensity distribution of different derivative orders of CCADBs on the initial plane. As we can see that the intensity distribution of the CCADBs has circular symmetry, and the areas where light energy is concentrated are gradually transferred to the outer ring with the increase of the derivative order n. In order to better observe the intensity characteristics, the one-dimensional intensity distributions along the radial direction are also shown in Fig. 2. It can be clearly found that as n increases, the radius of the region with zero light intensity in the middle of the beam gradually increases, and the bright and dark rings become more and more dense. Except for the 0^{th}-order differential beam, the maximum intensity of the CCADB gradually increases with n goes up.

3.2. Focal length, focal depth, and K-value

The focal length, focal depth, and K-value of CCADBs are three important physical quantities in optical tweezers and particle manipulation applications. The focal length and focal depth determine the working distance and range, respectively. The K-value represents the autofocusing ability of CCADBs, and it determines the trapping stiffness of the particle. Usually, the CCADBs used in optical tweezers and particle manipulation must be small enough to capture and manipulate a specific particles. Therefore, the propagation dynamics of the CCADBs need to be studied

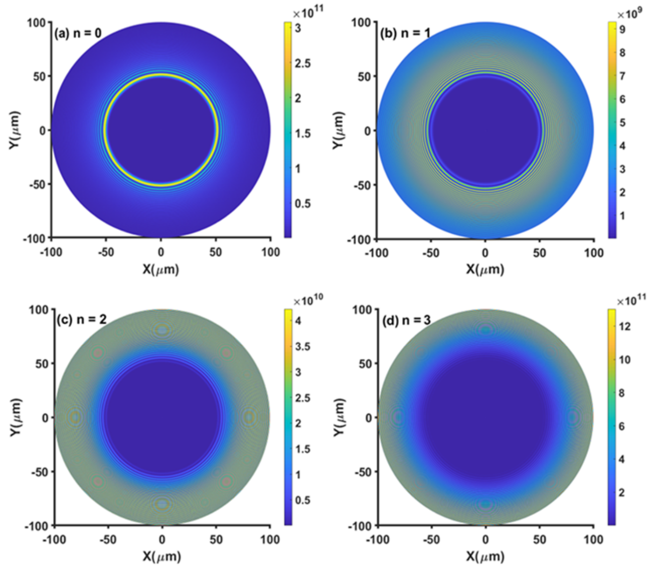

Fig. 1. Intensity distribution of different derivative orders of CCADBs on the initial plane.

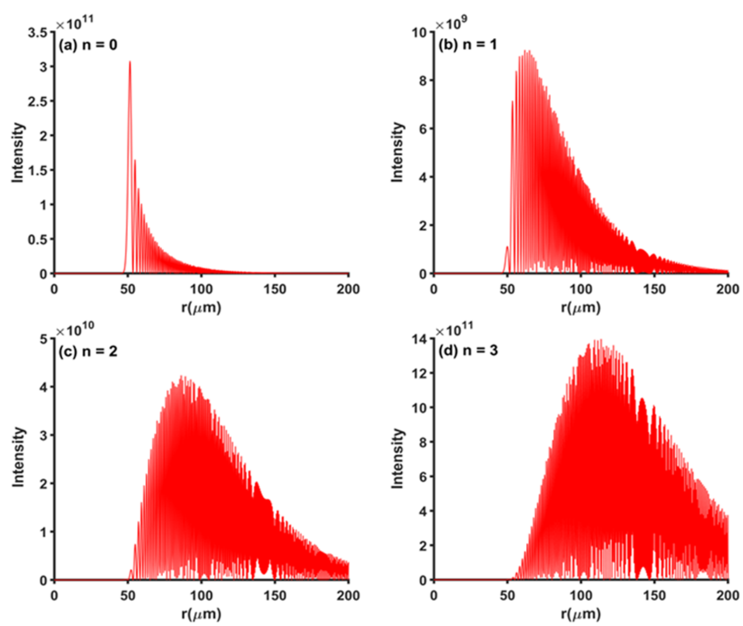

Fig. 2. Intensity distribution along the radial direction on the initial plane.

based on the nonparaxial propagation theory. The paraxial propagation model is no longer sufficiently accurate in this case.

To better compare and analyze the propagation dynamics of CCADBs in the case of paraxial and nonparaxial propagation models, we show the side-view intensity distribution along the propagation direction in Fig. 3. As seeing, the intensity profiles in both cases are obviously different. Although the intensity distribution under these two models shows abruptly autofocusing effect, the light intensity along the optical axis shows serious oscillation in the paraxial model while the oscillation disappears in the nonparaxial model. The difference of intensity profile is mainly attributed to the influence of the E_z component. In addition, when the derivative order n is the same, the size of the focus spot along the transverse direction is approximately equal in the paraxial and nonparaxial model. The effect of n value on the transverse focusing spot size is very small. The result can be clearly seen from the inset image of each subimage in Fig. 3, where all inset images are marked by the white dotted line box. And these inset images correspond to the effect that the focusing spot profile is magnified 4.36 times in equal proportions, respectively.

The distance from the initial plane ($z = 0$) to the position of maximum intensity is defined as the focal length of CCADBs. According to the calculation results, the focal lengths in the paraxial model are 261.9, 261.7, 261.7, and 261.7 µm, respectively, as the derivative order n increases from 0 to 3. In terms of the numerical size, the focal lengths are nearly independent of the order of derivative n, which is in agreement with the conclusion in the literature [5]. Corresponding to the nonparaxial model, the focal lengths are 237.3, 233.5, 232.1, and 230.9 µm, respectively. It shows that the focal length decreases gradually as n increases. Moreover, the focal lengths obtained by the nonparaxial model are significantly shorter than that obtained by the paraxial model. So, the differential order n can be used to elastically regulate the focal length when the CCADBs are applied to particle manipulation and other cases involving nonparaxial propagation.

To assess the focus depth and autofocusing ability of the CCADBs, another physical quantity named the relative on-axis intensity is defined by the ratio of the on-axis light intensity I (0, z) to the maximum intensity on the initial plane I_{0max}. Figure 4 presents the relative on-axis intensity distribution curve with different derivative orders under the paraxial and nonparaxial propagation. As we can see that in the paraxial model the curves have several peaks with gradually decreasing intensity, but only a single peak with a long tail in the nonparaxial model. In this paper, the full width at half maximum (FWHM) of the single peak of the relative on-axis intensity curve obtained from the nonparaxial model is regarded as the focal depth of CCADBs. Depending on the calculation results, the focal depths corresponding to the increase of n from 0 to 3 are 88.90, 21.20, 11.95, and 9.12 µm, respectively. This means that the focal depth decreases obviously as the order of differentiation increases.

In optical tweezers applications, the autofocusing ability can reflect the gradient force or trapping stiffness of the CCADBs on a dielectric particle to a certain extent. It can be described by a ratio of $K = I_{fmax}/ I_{0max}$, where I_{fmax} and I_{0max} correspond to the maximum light intensity at the focal plane and the initial plane, respectively. From the Fig. 4, it can be seen that the K-value in the nonparaxial model is significantly lower than that of the paraxial model when the derivative order n is the same. As n increases from 0 to 3, the K-value obtained in both calculation models increases, which prove that the autofocusing ability is enhanced. Beyond that, with the increase of n, the K-value obtained by the two kinds of calculation models tends to be closer to each other. In addition, it is also worth noting that the increase of n value can greatly increase K-value, which is beneficial to greatly regulating the trapping stiffness of particles in the application of optical tweezers. Based on the above results, it can be clearly seen that there are significant differences in the propagation characteristics of the CCADBs in paraxial and nonparaxial propagation models. Therefore, it is particularly important to study the non-paraxial propagation characteristics of the CCADBs in the field of optical tweezers and other applications involving non-paraxial propagation.

Optics EXPRESS

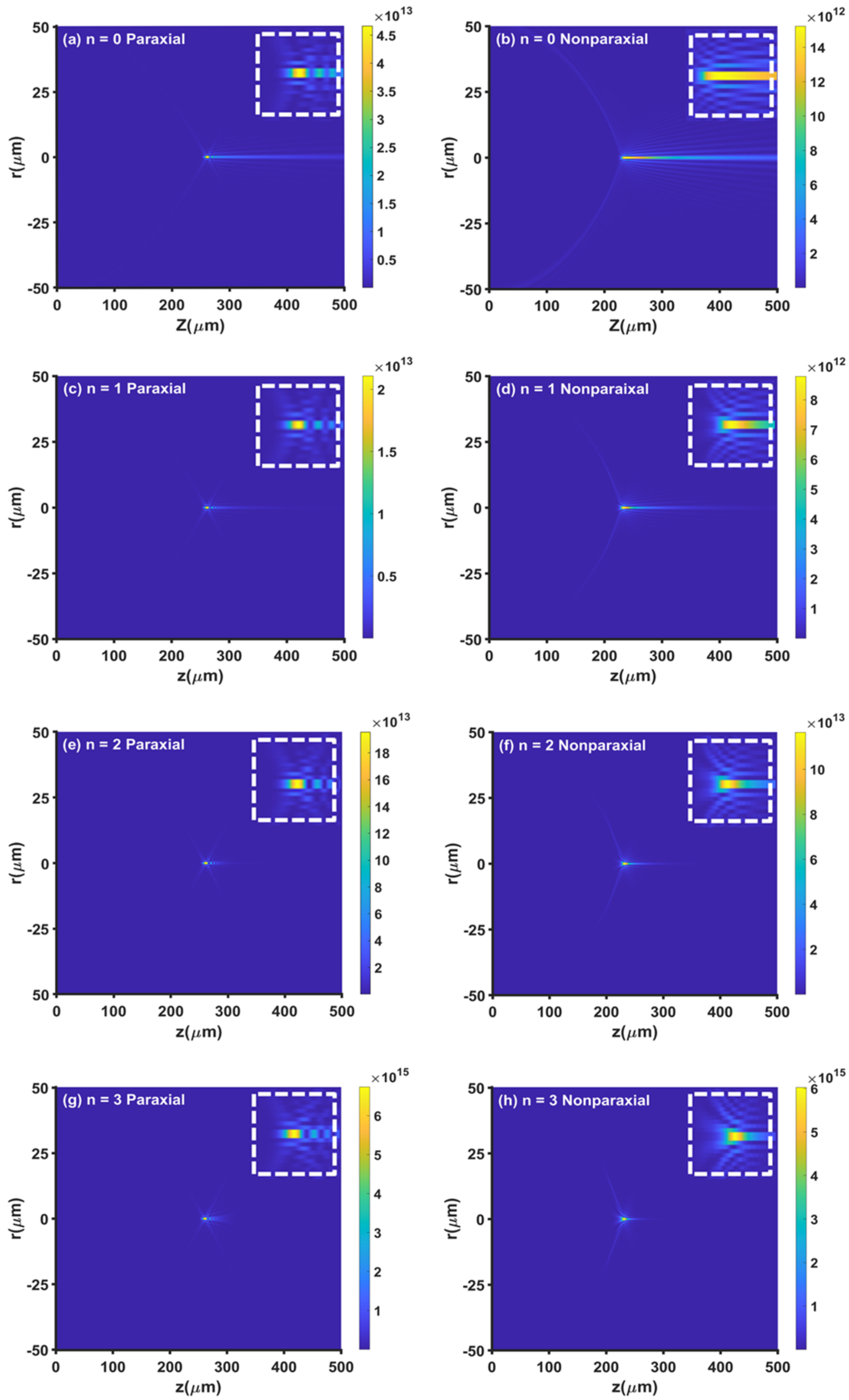

Fig. 3. Side-view intensity distribution along the propagation direction of the CCADBs in the paraxial and nonparaxial propagation models.

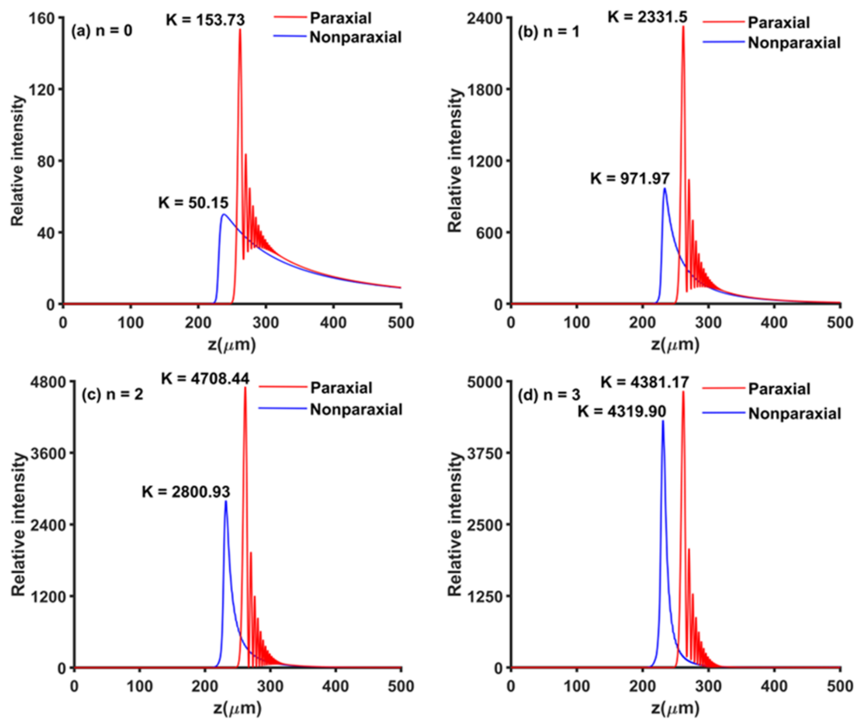

Fig. 4. Relative on-axis intensity of the CCADBs under paraxial and nonparaxial propagation.

3.3. Influence of the chirp parameter on propagation dynamics

The chirp factor is a useful physical quantity to control the propagation dynamics of the laser beam [22–26]. By introducing different chirp quantity (from c1 to c5) in the CADBs, we find the focal length, focal depth, and K-value can be greatly affected under the nonparaxial propagation model. Figure 5 shows the relative on-axis intensity distribution curve of the CADBs under different chirp parameters, where the case of unchirp ($c3 = 0$) modulation is also given again in order to distinguish the influence of positive chirp and negative chirp.

From Fig. 5, we can obviously see that for the CADBs with any derivative orders ($n = 0$, 1, 2, and 3), the negative chirp quantity make the focal position close to the source plane ($z = 0$), and the larger the absolute value of the negative chirp is, the closer it is. Through accurate calculation, we can also find that the focal depth decreases with the increase of the absolute value of the negative chirp, and the peak section of the curve becomes finer and sharper. According to the K-value data presented, the negative chirps obviously tend to enhance the autofocusing effect through compressing the focal length, and the K-value is remarkably increased with the increase of absolute value of negative chirp.

In stark contrast to the negative chirp above, the relative on-axis intensity evolution of the CADBs with the positive chirp parameters is in an almost opposite change. With the increase of chirp value, the focal length of CADBs with different n value becomes longer and the K-value decreases. According to the change trend of the relative on-axis intensity curve, in fact, it can be predicted that the autofocusing ability may be completely eliminated when the positive chirp coefficient increases to a certain extent. The reason for this result can be interpreted as the positive chirp can prevent the acceleration of the radial profile toward the center position. Compared with the modulation effect of the derivative order n, the chirp factor has a more delicate regulation

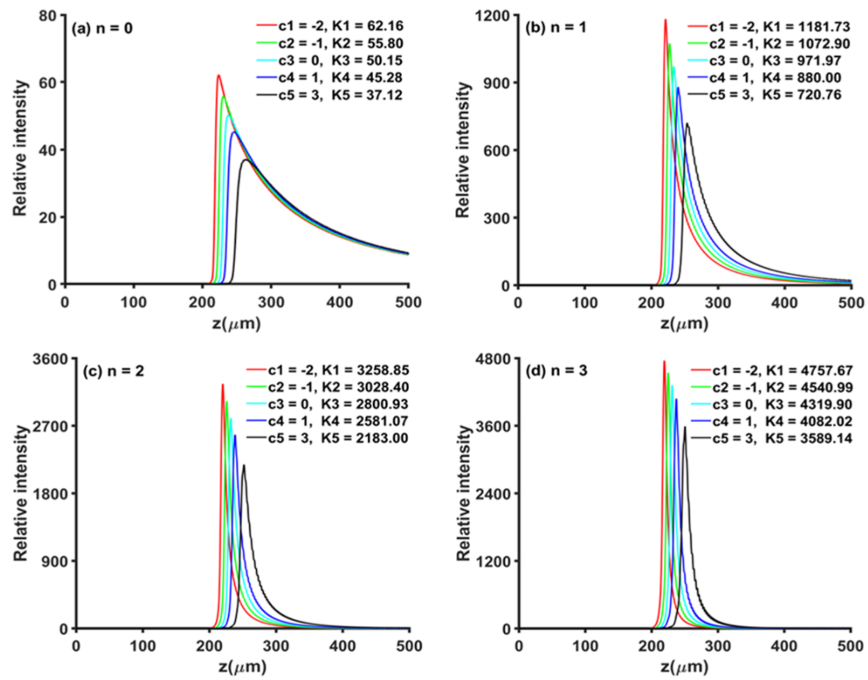

Fig. 5. Relative on-axis intensity of the chirped CADBs under the nonparaxial propagation.

effect on the optical field propagation characteristics of CADBs. In other words, we can achieve precise regulation of the capture stiffness of particles by fine-tuning the chirp factor in optical tweezers applications.

4. Radiation forces of CCADBs on a Rayleigh particle

In this section, we investigate the radiation force of CCADBs on a Rayleigh particle in the nonparaxial propagation model. The calculation principle of the radiation force are described in detail, and several numerical examples are performed based on the parameters set in the previous section, where $a = 0.2$, $b = 0.15$, $c = 0$, $w_0 = 10\,\mu\text{m}$, $r_0 = 50\,\mu\text{m}$, $\lambda = 632.8\,\text{nm}$, and the incident power is set to 1 W.

4.1. Theoretical analysis of the radiation force calculation

Rayleigh dielectric particle can be considered as a point dipole in the light fields. So the Rayleigh scattering model is used to calculate the radiation force of CCADBs on the Rayleigh dielectric particle in this paper. The time-averaged version of the Poynting vector is an important and measurable physical quantity in evaluating radiation force and is given by [27]

$$\left\langle \vec{S}(\vec{r}, t) \right\rangle_t = \frac{1}{2}\text{Re}[\vec{E} \times \vec{H}]\,. \tag{10}$$

Substituting Eqs. (4), (6) into (10), and using the relationship between electric and magnetic fields, we can obtain the time-averaged version of the Poynting vector as follows

$$\left\langle \vec{S}(\vec{r}, t) \right\rangle_t = \frac{n\varepsilon_0 c}{2}|E_x|^2 \vec{e}_z + \frac{n\varepsilon_0 c}{2}|E_x||E_z|\vec{e}_x. \tag{11}$$

Optics EXPRESS

The gradient force F_g and scattering force F_s are two kinds of main radiation force on the Rayleigh particle. They can be calculated by the following two equations

$$\vec{F}_g = \frac{2\pi n_m R^3}{c}\left(\frac{\eta^2-1}{\eta^2+1}\right)\nabla(\vec{E}\cdot\vec{E}^*), \tag{12}$$

$$\vec{F}_s = \frac{8\pi n_m R^6 k_0^4}{3c}\left(\frac{\eta^2-1}{\eta^2+2}\right)^2\left\langle\vec{S}(\vec{r},t)\right\rangle, \tag{13}$$

where R is the radius of the dielectric particle, $\eta = n_p/n_m$, is the relative refractive index of the particle, n_m and n_p are the refractive index of the particle and the surrounding medium respectively. k_0 is the vacuum wave number, c is the speed of light. Thus, the gradient force and scattering force of x and z components can be expressed as follows

$$F_{gx} = \frac{2\pi n_m R^3}{c}\left(\frac{\eta^2-1}{\eta^2+1}\right)\frac{\partial}{\partial x}(|E_x|^2+|E_z|^2), \tag{14}$$

$$F_{gz} = \frac{2\pi n_m R^3}{c}\left(\frac{\eta^2-1}{\eta^2+1}\right)\frac{\partial}{\partial z}(|E_x|^2+|E_z|^2), \tag{15}$$

$$F_{sx} = \frac{8\pi n_m R^6 k_0^4}{3c}\left(\frac{\eta^2-1}{\eta^2+2}\right)^2\cdot\frac{n\varepsilon_0 c}{2}|E_x|\cdot|E_z|, \tag{16}$$

$$F_{sz} = \frac{8\pi n_m R^6 k_0^4}{3c}\left(\frac{\eta^2-1}{\eta^2+2}\right)^2\cdot\frac{n\varepsilon_0 c}{2}|E_x|^2. \tag{17}$$

In calculation, we assume the surrounding medium is water (refractive index $n_m = 1.33$), and the dielectric particle is the glass microsphere (refractive index $n_p = 1.59$) with a radius of $R = 30$ nm.

4.2. Radiation forces of the unchirped CADBs on Rayleigh glass microsphere

When the incident power of the unchirped CADBs is set to 1 W, the radiation force exerted on the Rayleigh glass microsphere along the optical axis can be calculated by using the mathematical expression: $F_z = (F_{\mathrm{scat}})_z + (F_{\mathrm{grad}})_z$. For different derivative order n, the corresponding radiation force distribution curves are shown in Figs. 6(a)-(d), respectively. F_z value on the black dotted line is equal to 0. In order to clarify the equilibrium point, we have given a zoomed figure in the inset, where the curve in the ellipse clearly shows the F_z distribution near the theoretical mechanical equilibrium position point. The center of the small blue circle inserted in each subfigure represents the equilibrium point along the optical axis and it is also where the arrow points.

As seeing from Fig. 6(a), when $n = 0$, the radiation force generated by CADBs is hardly able to trap the particle, because the driving force along the optical axis forward is absolutely dominant. When n increase from 1 to 3, the positions of the equilibrium point are 235.7, 232.4 and 231.1 µm, respectively, which are slightly shifted in the opposite direction of the beam. In addition, as n increases, the radiation force F_z is significantly enhanced, and the share of radiation force along the opposite direction of propagation becomes more and more prominent, which is conducive to the stable capture of glass microsphere.

The transverse radiation force F_x at the equilibrium point on the optical axis can be calculated by using the mathematical expression: $F_x = (F_{\mathrm{scat}})_x + (F_{\mathrm{grad}})_x$. The corresponding calculation results are shown in Fig. 7, respectively, where we use the subscript r instead of x, just to be consistent with the previous statement in the second part of this paper. Unlike the radiant force F_z, the transverse radiant force F_r exhibits a high degree of symmetry. Similarly, the center of the small blue circle inserted in each subfigure represents the theoretical mechanical equilibrium

Optics EXPRESS

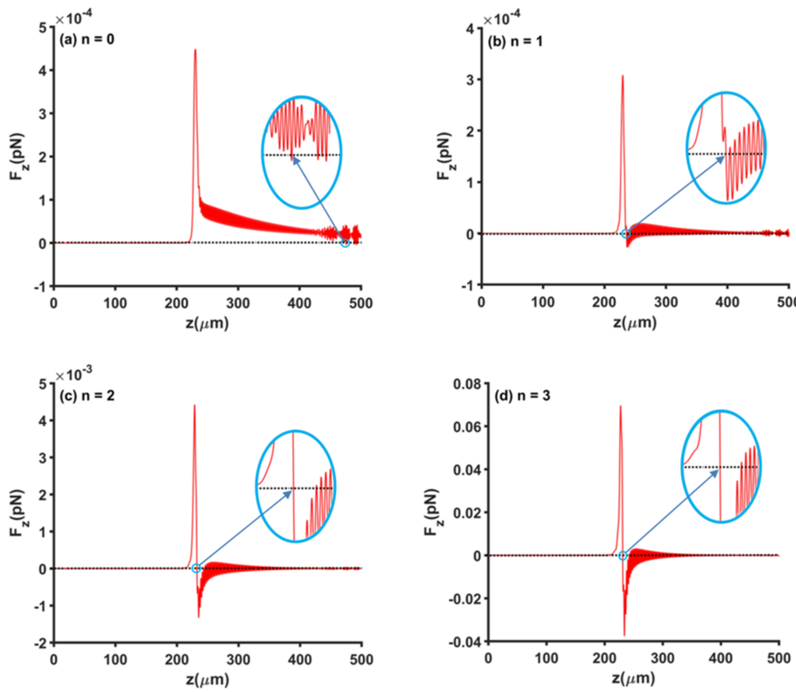

Fig. 6. Radiation forces on the Rayleigh glass microsphere along the optical axis.

point along the transverse direction. As seeing from Figs. 7(a)-(d), in numerical terms, F_r also increases as derivative order n increases. This means that the stiffness of the optical trap can be enhanced by choosing the proper derivate order.

4.3. Radiation forces of the chirped CADBs on Rayleigh glass microsphere

The chirp parameters can modulate the light field distribution of CADBs, so we investigate the influence of different chirp on the radiation force. Here the same chirp factors as before (c1 = -2, c2 = -1, c3 = 0, c4 = 1, and c5 = 3) are used in numerical calculation, and c3 = 0 indicates that CADB is unchirped, and its function here is to clearly distinguish the changes of radiation force under the modulation of positive and negative chirps. Figure 8 shows the radiation force distribution curves of different differential orders of CADBs on Rayleigh glass microsphere along the axis, under the different chirp factors. Especially, when $n = 0$, the radiation forces F_z are mainly forward thrust, and the forward thrust gradually decreases with the increasing of chirp factor from negative to positive. In this case, in fact, it is almost impossible for the microsphere to be stably trapped along the axial direction. As n goes from 1 to 3, the radiation force F_z shows an order of magnitude increase. In addition, we can also clearly see that the share of radiation force in the opposite direction of the optical axis become more and more prominent, which is more conducive to stable particle trapping. For any derivative order ($n = 1, 2, 3$), the equilibrium point is moved towards the direction of beam propagation and the magnitude of the radiation force is also reduced with the chirp factor changes from negative to positive. Meanwhile, the share of radiation force in the opposite direction of the optical axis gradually decreases as the chirp factor changes from -2 to 3. This means that if the chirp factor continues to increase, there will be no photomechanical equilibrium and the radiation force F_z will be unable to capture the particles.

For $n = 0$, the radiation force of the CADBs along the optical axis is not enough to capture the Rayleigh microsphere. Here we only investigate the transverse radiation force in the case of $n = 1$,

Optics EXPRESS

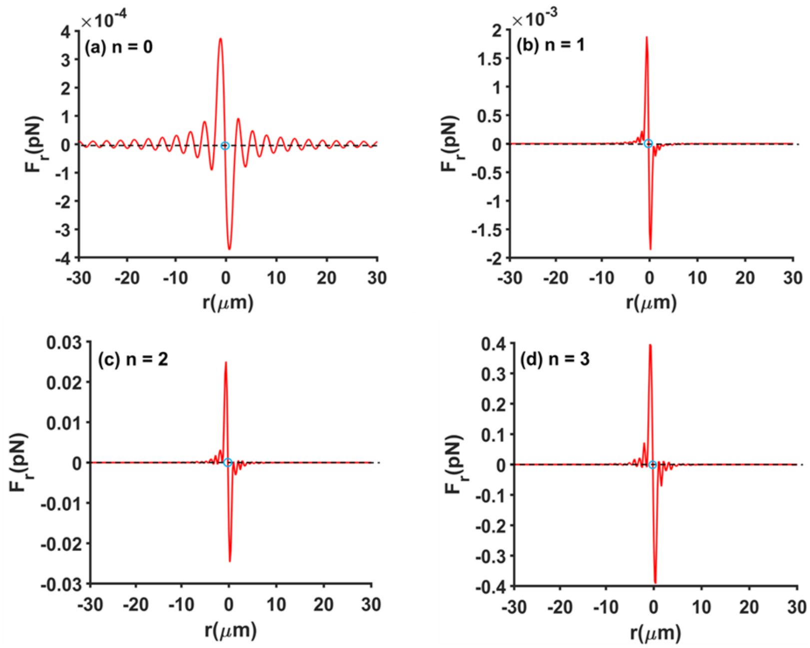

Fig. 7. Transverse radiation force at the equilibrium point on the optical axis.

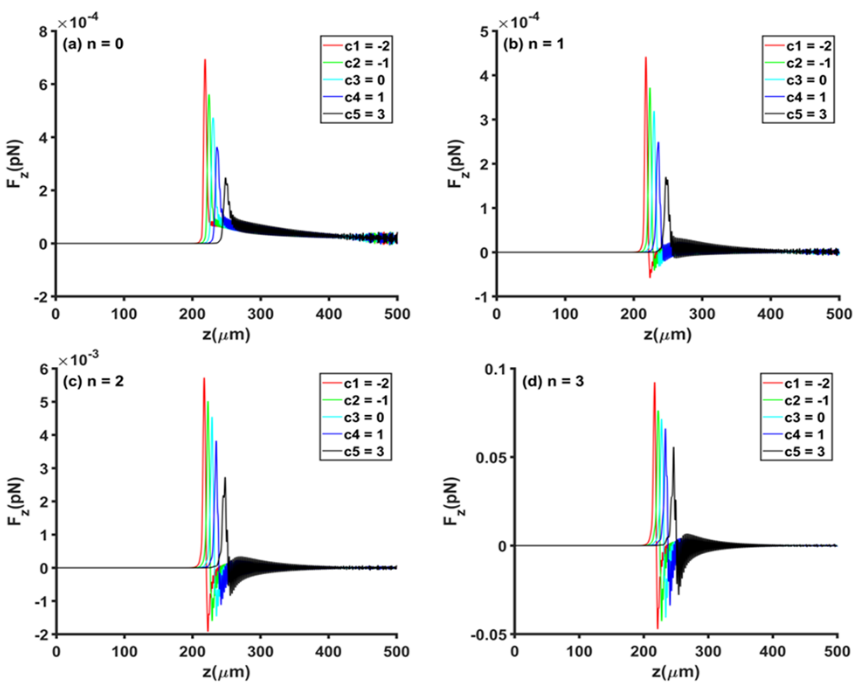

Fig. 8. Radiation forces along the optical axis with different chirp factor.

Optics EXPRESS

2, and 3. Figure 9 shows the transverse radiation force at the equilibrium point on the optical axis for different chirp factors. As seen, the transverse radiant force curves are basically symmetric with respect to the equilibrium point on the optical axis. In theory, the transverse photomechanical equilibrium point of the microsphere is consistent with the longitudinal equilibrium point. With the increase of derivative order n, the transverse radiation force increases by orders of magnitude. In addition, we can see that with the same n value, the transverse radiation force gradually weakens with the chirp factor increasing from -2 to 3, which is not conducive to stable capture of the microsphere. Therefore, both chirp parameter and derivative order have significant influence on the trapping force of microsphere.

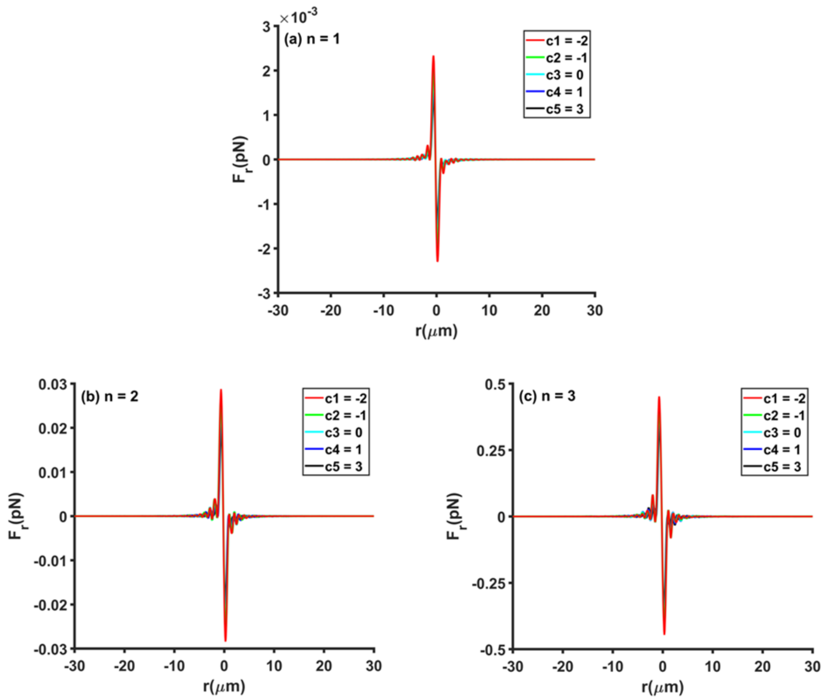

Fig. 9. Transverse radiation force at the equilibrium point with different chirp factor.

4.4. Stability analysis of microsphere capture

There are several necessary conditions for the stable trapping of glass microsphere. First, the backward longitudinal gradient force must be sufficient to overcome the forward scattering force. That means that the magnitude of F_z and F_r has a position equal to zero along the optical axis and the transverse direction, respectively, which is satisfied in our calculations, except $n = 0$. Second, F_z and F_r must be larger than the gravity of the particle. In our case, the gravity of the glass microsphere with a radius of 30 nm and a density of $(2.4\sim2.8) \times 10^3$ kg/m^3 is about $(2.7\sim3.1) \times 10^{-6}$ pN, which is also fulfilled. Third, the Brownian force must be much smaller than the trapping forces of the CADBs. The magnitude of the Brownian force can be expressed as $F_B = (12\pi\eta R k_B T)^{1/2}$, where η is the viscosity of the water ($\eta = 7.977 \times 10^{-4}$ Pa·s when $T = 300$ K), R is the radius of the glass microsphere and k_B is the Boltzmann constant. Then we get the magnitude of the Brownian force $F_B = 1.933 \times 10^{-3}$ pN. Compare the Brownian forces with the radiation forces F_z shown in Figs. 8, we can infer that when $n = 0$ and 1, the radiation force along the optical axis cannot achieve stable trapping of glass microspheres. When $n = 2$, the Brownian forces and radiation forces F_z are of the same order of magnitude, so the capture along the optical

Optics EXPRESS

axis can be achieved, but the captured glass microsphere is prone to escape from the interference by other factors. When $n = 3$, the radiation forces F_z are much larger than the Brownian force, so it is easy to realize the stable capture of glass microspheres along the optical axis. Based on the similar analysis, we can see from Fig. 9 that for $n = 1$, the magnitude of transverse radiation force F_r is comparable to that of the Brownian force, so it is also difficult to achieve stable capture effect. For $n = 2$ and 3, the transverse radiation forces F_r are significantly larger than the Brownian force, so the stable capture can be achieved easily. Besides the derivative order n, we also clearly find that chirp factor is another important physical quantity to regulate the radiation force F_z and F_r to a certain extent. Thus, the trapping stability of Rayleigh glass microsphere can be improved by changing the differential order or adjusting the chirp factor.

5. Conclusion

In conclusion, we have studied the nonparaxial propagation dynamics of the CADBs with different derivative orders and chirp parameters. The nonparaxial propagation dynamics are obviously different from those in the paraxial approximation model, which indicates that the study of nonparaxial propagation dynamics of CADBs is very important for its practical applications in optical tweezers and other aspects. The derivative order and chirp factor of the beam have significant and subtle effects on the nonparaxial propagation dynamics, respectively. Thus, the derivative order and chirp factor can be used to coarse and fine tune the capture effect of the beam on the Rayleigh microsphere respectively. It is worth noting that not all derivative order CCADBs can achieve stable trapping effect of Rayleigh microsphere, and it is necessary to choose suitable derivative order and chirp factor in practical application. Our research work will promote the more precise and flexible use of circular Airy derivative beams in optical tweezers, laser processing and other fields.

Funding. Key Laboratory of Optoelectronic Devices and Systems of Ministry of Education and Guangdong Province (GD202102); National Natural Science Foundation of China (62105049); Natural Science Foundation of Chongqing (cstc2021jcyj-msxmX1119); Science and Technology Research Project of Chongqing Education Commission (KJQN202100618); Doctoral program sponsored by Chongqing University of Posts and Telecommunications (E011A2022310); Chongqing Postdoctoral Research Fund Project (D63012022051).

Acknowledgments. All authors are very grateful to all the members of the Guangdong and Hong Kong Joint Research Centre for Optical Fibre Sensors and the Key Laboratory of Optoelectronic Devices and Systems of Ministry of Education and Guangdong Province, Shenzhen University, China for their support in this study.

Disclosures. The authors declare no conflicts of interest.

Data availability. Data underlying the results presented in this paper are not publicly available at this time but may be obtained from the authors upon reasonable request.

References

1. N. K. Efremidis and D. N. Christodoulides, "Abruptly autofocusing waves," Opt. Lett. **35**(23), 4045–4047 (2010).
2. D. G. Papazoglou, N. K. Efremidis, D. N. Christodoulides, and S. Tzortzakis, "Observation of abruptly autofocusing waves," Opt. Lett. **36**(10), 1842–1844 (2011).
3. Y. Jiang, X. Zhu, W. Yu, H. Shao, W. Zheng, and X. Lu, "Propagation characteristics of the modified circular Airy beam," Opt. Express **23**(23), 29834–29841 (2015).
4. J. D. Ring, J. Lindberg, A. Mourka, M. Mazilu, K. Dholakia, and M. R. Dennis, "Auto-focusing and self-healing of Pearcey beams," Opt. Express **20**(17), 18955–18966 (2012).
5. A. Zannotti, F. Diebel, M. Boguslawski, and C. Denz, "Optical catastrophes of the swallowtail and butterfly beams," New J. Phys. **19**(5), 053004 (2017).
6. H. Teng, Y. Qian, Y. Lan, and Y. Cai, "Abruptly autofocusing circular swallowtail beams," Opt. Lett. **46**(2), 270–273 (2021).
7. S. Zhang, J. Zhou, M. Zhong, and L. Gong, "Nonparaxial structured vectorial abruptly autofocusing beam," Opt. Lett. **44**(11), 2843–2846 (2019).
8. Q. Jiang, Y. Su, Z. Ma, Y. Li, and W. Zheng, "Nonlinear manipulation of circular Airy beams," Appl. Phys. B **125**(6), 105 (2019).
9. G. Zhou, R. Chen, and G. Ru, "Airyprime beams and their propagation characteristics," Laser Phys. Lett. **12**(2), 025003 (2014).

10. O. Vallée and S. Manuel, *Airy Functions and Applications to Physics* (Imperial College Press, 2010).
11. X. Zang, W. Dan, Y. Zhou, H. Lv, F. Wang, Y. Cai, and G. Zhou, "Abruptly autofocusing of generalized circular Airy derivative beams," Opt. Express **30**(3), 3804–3818 (2022).
12. H. Wu, C. Jiang, A. Ren, T. Dong, and X. Cui, "Single-fiber optical tweezers for particle trapping and axial reciprocating motion using dual wavelength and dual mode," Opt. Commun. **517**, 128333 (2022).
13. X. Zhang, L. Gong, G. Rui, J. He, Y. Cui, and B. Gu, "Effect of the thermal–optical nonlinearity on optical trapping Rayleigh particles," Opt. Commun. **495**, 127071 (2021).
14. C. J. Bustamante, Y. R. Chemla, S. Liu, and M. D. Wang, "Optical tweezers in single-molecule biophysics," Nat. Rev. Methods Primers **1**(1), 25 (2021).
15. R. Zhu, T. Avsievich, A. Popov, and I. Meglinski, "Optical tweezers in studies of red blood cells," Cells **9**(3), 545 (2020).
16. X. Chen, D. Deng, J. Zhuang, X. Yang, H. Liu, and G. Wang, "Nonparaxial propagation of Abruptly autofocusing circular Pearcey Gaussian beams," Appl. Opt. **57**(28), 8418–8422 (2018).
17. Z. Mei and D. Zhao, "Nonparaxial analysis of vectorial Laguerre-Bessel-Gaussian beams," Opt. Express **15**(19), 11942–11951 (2007).
18. G. Zhou, Y. Xu, and Y. Zhou, "Non-paraxial propagation of a circular Lorentz-Gauss vortex beam," J. Opt. Soc. Am. A **36**(7), 1221–1228 (2019).
19. B. Gu and Y. Cui, "Nonparaxial and paraxial focusing of azimuthal-variant vector beams," Opt. Express **20**(16), 17684–17694 (2012).
20. M. Guizar-Sicairos and J. C. Gutirrez-Vega, "Computation of quasi-discrete Hankel transforms of integer order for propagating optical wave fields," J. Opt. Soc. Am. A **21**(1), 53–58 (2004).
21. L. Yu, M. Huang, M. Chen, W. Chen, W. Huang, and Z. Zhu, "Quasi-discrete Hankel transform," Opt. Lett. **23**(6), 409–411 (1998).
22. K. Guo, J. Xie, G. Chen, Y. Wu, Y. Liang, S. Hong, F. Ye, J. Zhang, and D. Deng, "Abruptly autofocusing properties of the chirped circular Airy Gaussian vortex beams," Opt. Commun. **477**, 126369 (2020).
23. X. Chen, D. Deng, G. Wang, and X. Yang, "Abruptly autofocused and rotated circular chirp Pearcey Gaussian vortex beams," Opt. Lett. **44**(4), 955–958 (2019).
24. J. Xie, J. Zhang, J. Ye, H. Liu, Z. Liang, S. Long, K. Zhou, and D. Deng, "Paraxial propagation of the first-order chirped Airy vortex beams in a chiral medium," Opt. Express **26**(5), 5845–5856 (2018).
25. J. Zhang, Z. Pang, L. Feng, T. Zhong, L. Wang, and D. Deng, "Propagation properties of the chirped Airy vortex beams through left-handed and right-handed material slabs," Chin. Opt. Lett. **15**, 060501 (2017).
26. X. Wu, Y. Peng, Y. Wu, H. Qiu, K. Chen, D. Deng, and X. Yang, "Nonparaxial propagation and the radiation forces of the chirped annular Bessel Gaussian beams," Results Phys. **19**, 103493 (2020).
27. H. Cheng, W. Zang, W. Zhou, and J. Tian, "Analysis of optical trapping and propulsion of Rayleigh particles using Airy beam," Opt. Express **18**(19), 20384–20394 (2010).